THE JOURNAL OF
PHYSICAL CHEMISTRY A

Article

pubs.acs.org/JPCA

Relative Intermolecular Orientation Probed via Molecular Heat Transport

Hailong Chen, Hongtao Bian, Jiebo Li, Xiewen Wen, and Junrong Zheng*

Department of Chemistry, Rice University, Houston, Texas 77005, United States

Supporting Information

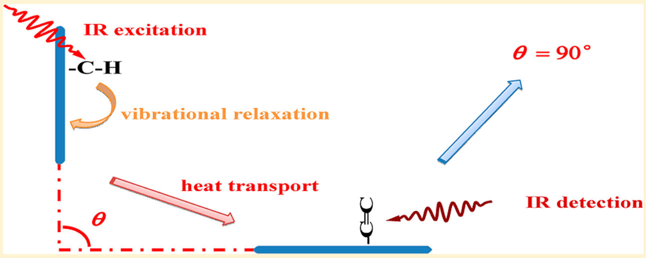

ABSTRACT: In this work, through investigating a series of liquid, glassy, and crystalline samples with ultrafast multiple-mode 2D IR and IR transient absorption methods, we demonstrated that the signal anisotropy of vibrational relaxation-induced heat effects is determined by both relative molecular orientations and molecular rotations. If the relative molecular orientations are randomized or molecular rotations are fast compared to heat transfer, the signal anisotropy of heat effects is zero. If the relative molecular orientations are anisotropic and the molecular rotations are slow, the signal anisotropy of heat effects can be nonzero, which is determined by the relative orientations of the energy source mode and the heat sensor mode within the same molecule and in different molecules. We also demonstrated that the correlation between the anisotropy value of heat signal and the relative molecular orientations can be quantitatively calculated.

1. INTRODUCTION

Fast molecular conformational fluctuations in condensed phases play critical roles in many important chemical and biological activities.[1,2] Monitoring real time three-dimensional molecular conformations is of great significance in understanding these activities, e.g., chemical reactions, protein foldings, and molecular recognitions. Nuclear magnetic resonance (NMR) methods have been successfully developed for this purpose.[3] However, their intrinsic low temporal resolution (longer than 10^{-6} s) provides only a longtime average.

The ultrafast multiple-dimensional vibrational spectroscopy techniques developed in the past decade have a sufficiently high temporal resolution (~100 fs) to reveal fast molecular information that NMR methods have difficulties to obtain.[4−13] However, because of technical difficulties and complex theoretical interpretations of molecular vibrational couplings and transfers, it is generally believed that ultrafast nonlinear vibrational spectroscopic methods are more suitable for investigating some specifically labeled molecular segments rather than the entire molecular structures. Recently, combining new technical designs and model system studies, we demonstrated that real time three-dimensional molecular conformations of some relatively simple molecular systems in condensed phases can be determined by the multiple-mode method by which vibrations covering the entire molecular space are simultaneously measured.[14−16] To resolve the 3D structure of a molecule, both lengths and relative orientations of its chemical bonds must be determined. Therefore, in order to achieve our ultimate goal of developing the ultrafast multiple-mode multiple-dimensional vibrational spectroscopy into a self-consistent molecular structural tool, we have designed experiments to explore its possibilities of acquiring these two types of molecular information. To explore its potential for determining interbond distances, we have conducted a series of experiments to investigate the correlations between mode-specific vibrational energy transfer kinetics and bond distances.[17−23] To explore its potential for determining relative bond orientations, we have conducted experiments to investigate the correlations between vibrational cross angles and corresponding chemical bond angles.[14,16] In principle, both mode-specific vibrational energy transfer and vibrational cross angle methods are suitable for determining both inter- and intramolecular structures. In reality, the two approaches are mainly applicable to intramolecular structures and some very strong intermolecular interactions, e.g., H-bonds and ionic interactions. At the current stage, they have difficulties in probing most relatively weak intermolecular interactions, because the vibrational couplings in these intermolecular interactions are too weak to provide signals with a sufficiently high signal/noise ratio. In many practical situations, e.g., crystals, guest/host interactions, and catalysts of asymmetric synthesis, the relative orientations of adjacent molecules which do not necessarily strongly interact with each other are important. In this work, we will introduce a new approach to probe the relative orientations of some molecules of which the intermolecular interactions are weak. The approach is based on the intermolecular vibrational relaxation-induced heat effects.

Special Issue: Prof. John C. Wright Festschrift

Received: December 21, 2012
Revised: February 25, 2013
Published: February 25, 2013

dx.doi.org/10.1021/jp312604v | *J. Phys. Chem. A* 2013, 117, 6052−6065

In a typical nonlinear vibrational spectroscopic measurement in condensed phases, the relaxation of a vibrational excitation into thermal motions results in a temperature increase within a short period of time in the sample within the focus spot.[15,17,24,25] The temperature increase can affect the sample in several ways,[15] i.e., altering the absorption coefficients of the vibrational modes, changing the populations of molecules in different substates, and/or shifting the local structures and chemical equilibrium following the temperature change; e.g., H-bonds become weaker at higher temperature.[26,27] As a result, these vibrational relaxation-induced heat effects produce new absorptions and bleachings at various temperatures in both temperature difference FTIR spectra and 2D IR spectra.[18] In this paper, we define "heat" as those thermal motions which include low frequency molecular vibrations, rotations, and translations induced by the excitation relaxation of a high frequency vibrational mode (denoted as "energy source mode") and the "heat effects" as the optical responses of high frequency vibrational modes (denoted as "heat sensor modes") to the thermal motions.

Similar to the internal vibrational relaxation processes studied with relaxation-assisted two-dimensional infrared (RA 2DIR) spectroscopy,[28−30] the theoretical basis of the intermolecular vibrational relaxation-induced heat transfer is not entirely clear. Generally speaking, the intermolecular vibrational relaxation-induced heat can be transferred from the original exited molecules to adjacent molecules at the time scales of fs (femtosecond) to ns (nanosecond), dependent on the vibrational lifetimes of modes involved in the intramolecular relaxation.[18,31] Once the molecules receive the heat energy, the absorption coefficients and frequencies of their vibrational modes and their chemical states will shift to new values because of the temperature change. The changes of molecular properties will result in new absorptions and bleachings in IR spectra which can be monitored in real time. In the relaxation-induced heating process, the heat source is from one vibrational mode of one molecule, and the sensor of the heat effects can be another vibrational mode of another molecule. In principle, the relative orientation and distance between the energy source mode and the heat sensor mode are correlated to the heat transfer kinetics. Such a correlation can be utilized to determine the relative orientation and distance of the two molecules to which the two vibrational modes belong.

In this work, we first simply introduce the generation mechanism of relaxation-induced heat and equations to calculate the anisotropy of the heat signal. Then, examples of a liquid and a crystal are used to demonstrate that a nonzero anisotropic value of relaxation-induced heat signal can exist in a sample where molecular orientations are anisotropic and molecular rotations are slow. In the last part of the work, we use three polystyrene samples with different molecular orientations: isotropic (amorphous glass) and anisotropic (crystal) to demonstrate that the correlation between the relative intermolecular orientation and the nonzero anisotropy value of the molecular heat transport signal can be quantitatively calculated.

2. EXPERIMENTS

The optical setup is similar but with a different probe pulse generation method to that described previously.[15,17] Briefly, a ps amplifier and a fs amplifier are synchronized with the same seed pulse. The ps amplifier pumps an OPA to produce ~0.8 ps (vary from 0.7 to 0.9 ps in different frequencies) mid-IR pulses with a bandwidth of 10−35 cm^{-1} in a tunable frequency range from 400 to 4000 cm^{-1} with energy 1−40 μJ/pulse (1−10 μJ/pulse for 400−900 cm^{-1} and >10 μJ/pulse for higher frequencies) at 1 kHz. Light from the fs amplifier is used to generate a high-intensity mid-IR and terahertz supercontinuum pulse with a duration of <100 fs in the frequency range from <400 to >3000 cm^{-1} at 1 kHz, with a modified terahertz generation method which is similar to those used in other groups.[32−35] Specifically, the collimated 800 nm beam from the fs amplifier is frequency doubled by passing through a type-I 150-μm-thick BBO crystal cut at 29.2° to generate 400 nm light. A dual wave plate is used to tune the relative polarizations of the 800 and 400 nm pulses, which operates as a full-wave plate at 400 nm and a half-wave plate at 800 nm. Temporal walkoff between two beams is compensated by inserting a 2-mm-thick BBO (cut at 55°) between the doubling crystal and the wave plate, where the 800 and 400 nm pulses propagate at orthogonal polarizations with different velocities in the delay plate.[36,37] The supercontinuum pulse is generated by focusing the two copropagating beams on air. In nonlinear IR experiments, the ps IR pulse is the excitation beam (the excitation power is adjusted on the basis of need, and the interaction spot varies from 100 to 500 μm). The supercontinuum pulse is the probe beam which is frequency resolved by a spectrograph (resolution is 1−3 cm^{-1} dependent on the frequency), yielding the detection axis of a 2D IR spectrum. Scanning the excitation frequency yields the other axis of the spectrum. Two polarizers are added into the detection beam path to selectively measure the parallel or perpendicular polarized signal relative to the excitation beam. The whole setup included frequency tuning is computer controlled.

KSeCN, D_2O, atactic polystyrene, and L-cysteine were purchased from Aldrich and used as received. The raw material of syndiotactic polystyrene (sPS) was produced and kindly supplied by Idemitsu Kosan Co. Ltd., Japan. Amorphous sPS films were prepared by rapidly quenching melt films in an ice−water bath. The crystalline sPS films were prepared by slowly cooling melt films down to room temperature according to the literature.[38] All samples for 2D IR measurements were contained in sample cells composed of two CaF_2 windows separated by a Teflon spacer. All the measurements were carried out at room temperature (21 °C).

Density functional theory (DFT) calculations were used to convert atomic coordinates (relative atomic orientations) into vibrational coordinates (relative vibrational orientations). The DFT calculations were carried out using Gaussian 09. The level and basis set used were Becke's three-parameter hybrid functional combined with the Lee−Yang−Parr correction functional, abbreviated as B3LYP, and 6-311++G(d,p).

3. SIGNAL GENERATION MECHANISM AND ANISOTROPY

3.1. Generation Mechanism of Vibrational Relaxation-Induced Heat.

The vibrational relaxation-induced heat effects described in this work refer to the optical absorptions and bleachings caused by the thermal motions due to the relaxation of vibrational excitation of high frequency modes (>200 cm^{-1}) into low frequency modes and the dissipations of the resulting low frequency excitations. The phenomenon can be monitored in real time with ultrafast nonlinear vibrational spectroscopic methods.[17,18,24,27,39,40] The average results of vibrational relaxation-induced heat effects are identical to the differences of FTIR spectra at various temperatures.[17,18,27,40] Figure 1

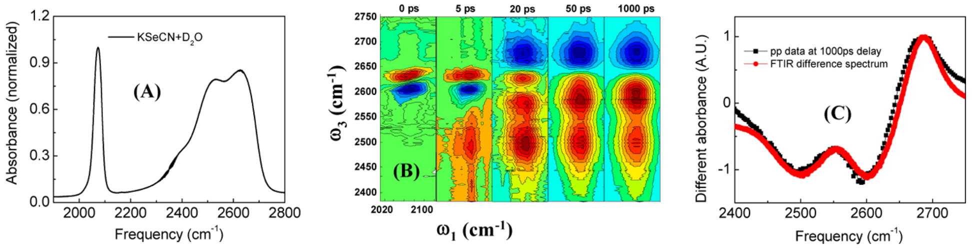

Figure 1. Spectra of a saturated KSeCN/D$_2$O solution (molar ratio ~1/2.5): (A) FTIR spectrum at room temperature showing the CN 0−1 transition peak of SeCN$^-$ at ~2070 cm^{-1}, the OD 0−1 transition peak of D$_2$O from ~2400 to ~2800 cm^{-1}, and a combination band (possibly C−N plus Se−C stretches) of SeCN$^-$ at ~2635 cm^{-1}; (B) 2D IR spectra (each contour represents 10% intensity change) showing the time evolutions of new absorptions (blue) and bleachings (red) in the OD frequency range (ω_3 = 2400−2750 cm^{-1}) induced by the vibrational relaxation of CN excitation at ~2070 cm^{-1} (ω_1 = 2070 cm^{-1}); (C) the temperature difference FTIR spectrum (spectrum at 68 °C − spectrum at 22 °C, red) and a slice cut (black) of panel 1000 ps in part B along the ω_3 axis at ω_1 = 2070 cm^{-1}, showing that the spectral changes caused by heat effects in 2D IR can be detected by temperature difference FTIR.

displays a typical example of vibrational relaxation-induced heat effects monitored with 2D IR and temperature difference FTIR.

Figure 1A is the FTIR spectrum of a saturated KSeCN/D$_2$O solution (molar ratio ~1/2.5) at room temperature. The CN stretch 0−1 transition frequency of SeCN$^-$ is at ~2070 cm^{-1}. The OD stretch 0−1 transition of D$_2$O has a very broad peak from ~2400 to 2800 cm^{-1}. The peak at ~2635 cm^{-1} which can also be clearly seen in a KSeCN/H$_2$O solution is assigned to a combination band (possibly the CN stretch plus the Se−C stretch) of SeCN$^-$. Figure 1B displays the waiting time dependent 2D IR spectra of the same sample by exciting the CN stretch of SeCN$^-$ and detecting responses in the frequency range 2400−2750 cm^{-1}. At a short waiting time, e.g., 0 ps, a peak pair shows up in the spectrum. These two peaks are from the vibrational coupling between the CN stretch and the combination band at ~2635 cm^{-1}, similar to those intramolecular vibrational couplings previously observed.[4,14] The coupling between CN and OD is too weak to be observed. At longer waiting times, the excitation of CN stretch of which the lifetime has a fast component of ~4 ps (22%) and a slow component of ~100 ps (78%) begins to relax into heat and raise the local temperature. As the temperature increases, the transition dipole moments of OD stretches change, and some hydrogen bonds in the solution break and some new bonds form, resulting in new absorptions (blue) and bleachings (red) in 2D IR spectra. In Figure 1B, at 5 ps, some of the heat effects (red peaks at ~2500 cm^{-1}) are already visible. At 20 ps, the heat effects (the blue peak at ~2680 cm^{-1}, red peaks at 2580 and 2480 cm^{-1}) are remarkable. At 50 ps, when the relaxation of CN excitation has not completed, the heat effect is already much larger than the vibrational coupling peaks so that only the heat effect is clearly visible. The spectral pattern of the heat effects in 2D IR remains essentially constant to the longest waiting time, 1000 ps, in our experiments. Because the spectral changes observed from 2D IR measurements are in nature caused by the temperature increase, such changes should also be observed by comparing FTIR spectra of the same sample at room temperature and at a higher temperature. Figure 1C displays the temperature difference FTIR spectrum (spectrum at 68 °C − spectrum at 22 °C, red) and a slice cut (black) of panel 1000 ps of part B along the ω_3 axis at ω_1 = 2070 cm^{-1}. The two curves are essentially identical, verifying that the spectral changes in 2D IR spectra in Figure 1B are from the temperature increase because of the relaxation of CN excitation.

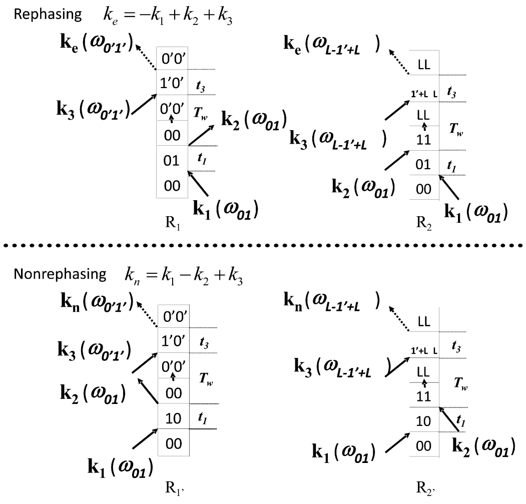

Figure 2. Feynman diagrams contributing to the vibrational relaxation-induced heat effects: bleaching (R_1 and $R_{1'}$) and absorption (R_2 and $R_{2'}$). 0 and 1 represent the ground state and the first excited state of the energy source mode—the initially vibrationally excited mode by laser, e.g., the CN stretch in Figure 1, respectively. 0′ and 1′ represent the ground state and the first excited state of the heat sensor mode—the mode which has optical responses to the heat, e.g., the OD stretch in Figure 1, respectively. L represents the excited states of low frequency modes (modes of heat) which accept energy from the relaxation of the energy source mode.

The vibrational relaxation-induced heat effects can be explained with Feynman diagrams shown in Figure 2, following the third order optical signal generation mechanism.[15,24] The 2D IR signals in our experiments are from the pump/probe scheme where the first two excitation beams k_1 and k_2 are collinear, and the third excitation beam k_3 and the local oscillator are also collinear. Therefore, both rephasing ($k_e = -k_1 + k_2 + k_3$, k_i is the wave vector of light pulse i) and nonrephasing ($k_n = k_1 - k_2 + k_3$) phase match conditions contribute the signals experimentally observed. In the diagrams in Figure 2, 0 and 1 respectively represent the ground state and the first excited state of the energy source mode—the initially vibrationally excited mode by laser, e.g., the CN stretch in Figure 1. 0′ and 1′ respectively represent the ground state and the first excited state of the heat sensor mode—the mode which has optical responses to the heat, e.g., the OD stretch in Figure 1. L represents the excited state(s) of low frequency modes (modes of heat) which accept energy from the relaxation of the energy source mode. Diagrams R_1 (rephasing) and $R_{1'}$ (nonrephasing) describe the process of heat-induced bleaching. They can be qualitatively understood in the following way. The first beam creates a coherence (superposition) between the ground state and the first excited state of the energy source mode which is oscillating during the t_1 period between the first two interactions. The coherence provides information for the excitation frequency ω_1. The second interaction excites some of the molecules to the first excited state, resulting in a population hole in the ground state. During the T_w period, the vibrational excitation begins to relax, and the excited molecules gradually go back to the ground state (hole recovered) as the relaxation heat dissipates to other molecules. At the same time, other molecules receive the heat and are excited so that ground state holes are generated in them. The process therefore looks like the exchange of ground state hole between two species. After the process, there are ground state holes in another species (heat sensor). The third pulse can then produce coherence between the ground state and the first excited state of the sensor mode to provide the detection frequency ω_3. This explains the generation of red peaks at 2400−2600 cm^{-1} at longer waiting times in Figure 1. ω_1 of these peaks is 2070 cm^{-1} which is the 0−1 transition frequency of the CN stretch, indicating that the energy source is the CN excitation. The relaxation of CN excitation heats up adjacent water molecules and generates ground state holes of the OD stretch, resulting in bleaching signals in the frequency range of the OD 0−1 transition detected as ω_3. If delta pulses are assumed,[41] 2D IR or pump/probe signals from diagrams R_1 and $R_{1'}$ can be expressed as

$$S_{R_1} \propto \cos\theta_{E_1/\mu_{01}} \cos\theta_{E_2/\mu_{01}} \cos\theta_{E_3/\mu_{0'1'}} \cos\theta_{E_s/\mu_{0'1'}} {\mu_{01}}^2 {\mu_{0'1'}}^2 \mathrm{e}^{i\omega_{01}t_1} \mathrm{e}^{-i\omega_{0'1'}t_3} \cdot \Gamma_{R_1}(t_1, T_\mathrm{w}, t_3) \cdot \exp[g_{R_1}(t_1, T_\mathrm{w}, t_3)] \tag{1}$$

and

$$S_{R_{1'}} \propto \cos\theta_{E_1/\mu_{01}} \cos\theta_{E_2/\mu_{01}} \cos\theta_{E_3/\mu_{0'1'}} \cos\theta_{E_s/\mu_{0'1'}} {\mu_{01}}^2 {\mu_{0'1'}}^2 \mathrm{e}^{i\omega_{01}t_1} \mathrm{e}^{i\omega_{0'1'}t_3} \cdot \Gamma_{R_{1'}}(t_1, T_\mathrm{w}, t_3) \cdot \exp[g_{R_{1'}}(t_1, T_\mathrm{w}, t_3)] \tag{2}$$

where $\Gamma(t_1, T_\mathrm{w}, t_3)$ is a time-damping factor whose details depend on the kinetic models. $g(t)$ is a line-broadening function, μ_{01} is the transition dipole moment of the 0−1 transition of the energy source mode, and $\mu_{0'1'}$ is the transition dipole moment of the 0−1 transition of the heat sensor mode. $\omega_1 = \omega_{01}$ is the 0−1 transition frequency of the energy source mode. $\omega_3 = \omega_{0'1'}$ is the 0−1 transition frequency of the heat sensor mode. $\theta_{E_i/\mu_{kl}}$ is the cross angle between the polarization direction of the ith electric field (including signal) and the direction of the transition dipole moment of μ_{kl}. In our experiments, $\cos\theta_{E_1/\mu_{01}} = \cos\theta_{E_2/\mu_{01}}$ and $\cos\theta_{E_3/\mu_{0'1'}} = \cos\theta_{E_s/\mu_{0'1'}}$. A similar situation holds for R_2 and $R_{2'}$.

Diagrams R_2 and $R_{2'}$ describe the process of relaxation-induced absorption. Similar to diagrams R_1 and $R_{1'}$, in R_2 and $R_{2'}$, the first pulse creates a superposition between the ground state and the first excited state of the energy source mode which provide the frequency information for ω_1. The second pulse creates a population on the first excited state of the energy source mode. During the T_w period, the first excited state population begins to relax into low frequency modes (heat) and dissipates to other molecules. The process produces excitations on these low frequency modes. While these low frequency modes are excited, the third pulse creates a superposition between the ground state and the first excited state of the heat sensor mode which provides the frequency information for ω_3. Signals from diagrams R_2 and $R_{2'}$ can be expressed as

$$S_{R_2} \propto -\cos\theta_{E_1/\mu_{01}} \cos\theta_{E_2/\mu_{01}} \cos\theta_{E_3/\mu_{L+0'\rightarrow L+1'}} \cos\theta_{E_s/\mu_{L+0'\rightarrow L+1'}} {\mu_{01}}^2 {\mu_{L+0'\rightarrow L+1'}}^2 \mathrm{e}^{i\omega_{01}t_1} \mathrm{e}^{-i\omega_{L+0'\rightarrow L+1'}t_3} \cdot \Gamma_{R_2}(t_1, T_\mathrm{w}, t_3) \cdot \exp[g_{R_2}(t_1, T_\mathrm{w}, t_3)] \tag{3}$$

and

$$S_{R_{2'}} \propto -\cos\theta_{E_1/\mu_{01}} \cos\theta_{E_2/\mu_{01}} \cos\theta_{E_3/\mu_{L+0'\rightarrow L+1'}} \cos\theta_{E_s/\mu_{L+0'\rightarrow L+1'}} {\mu_{01}}^2 {\mu_{L+0'\rightarrow L+1'}}^2 \mathrm{e}^{i\omega_{01}t_1} \mathrm{e}^{i\omega_{L+0'\rightarrow L+1'}t_3} \cdot \Gamma_{R_{2'}}(t_1, T_\mathrm{w}, t_3) \cdot \exp[g_{R_{2'}}(t_1, T_\mathrm{w}, t_3)] \tag{4}$$

where μ_{01} is the transition dipole moment of the 0−1 transition of the energy source mode and $\mu_{L+0'\rightarrow L+1'}$ is the transition dipole moment of the 0−1 transition of the heat sensor mode under the condition that the low frequency mode(s) L is (are) simultaneously excited. $\omega_1 = \omega_{01}$ is the 0−1 transition frequency of the energy source mode. $\omega_3 = \omega_{L+0'\rightarrow L+1'}$ is the 0−1 transition frequency of the heat sensor mode under the condition that the low frequency mode(s) L is (are) simultaneously excited.

In general, the excitations of these low frequency modes can change the vibrational frequencies and transition dipole moments of those high frequency modes, or change the chemical equilibrium of the system, e.g., forming a weaker H-bond in Figure 1. Therefore, the 0−1 transition frequencies of those high frequency modes detected with low frequency modes at excited states are different from those detected with low frequency modes at the ground state; e.g., $\omega_{L+0'\rightarrow L+1'}$ is different from $\omega_{0'1'}$. This explains the generation of the blue peak at ∼2680 cm^{-1} at longer waiting times in Figure 1. ω_1 of the peaks is 2070 cm^{-1} which is the 0−1 transition frequency of the CN stretch, indicating that the energy source is the CN excitation. The relaxation of CN excitation heats up adjacent water molecules and breaks some of the hydrogen bonds, shifting the OD 0−1 transition frequency from ∼2500 to ∼2680 cm^{-1} as detected in ω_3.

The heat effects described in this work are caused by the excitation relaxation of the energy source mode and the dissipation of thermal motions from the relaxation, different from the mode-specific vibrational energy transfer between the energy source mode and the probe mode which occurs before the relaxation of the source mode.[20,21] At waiting times much longer than the vibrational lifetimes of either mode, signals in 2D IR or pump/probe data are mainly from the heat effects. The detailed difference between these two processes has been described in our previous publications.[15,24]

3.2. Anisotropy of Vibrational Relaxation-Induced Heat Signal. From eqs 1−4, we can see that the signals of relaxation-induced heat effects depend on the heat transfer kinetics which is included in $\Gamma(t_1, T_\mathrm{w}, t_3)$. The heat transfer kinetics is correlated to the distance between the energy source and the heat sensor. In principle, the correlation can be utilized to determine the relative distance between the two molecules from the growth kinetics of heat effects. This is an interesting topic for future studies. In this work, we will focus on another aspect—anisotropy of the experimental signals from the heat effects. Equations 1−4 show that the heat signal is also dependent on the cross angles between the polarization directions of the excitation (E_1 and E_2) and detection (E_3) lights and the transition dipole moment directions of the energy source mode and the heat sensor mode. The signal will be maximized if both excitation and detection polarizations are respectively parallel to those of the two modes ($\theta_{E_i/\mu_{kl}} = 0$). In other words, the signal intensity of heat effects is correlated to the relative orientation of the energy source mode and the sensor mode, which can be experimentally determined by tuning the polarization angle between the excitation and detection pulses. Similar to the polarization selective fluorescence measurements,[42] if the heat transfer is isotropic and the molecular distribution within the laser focus spot is isotropic, the transition dipole moment cross angle $\theta(t)$ between the energy source mode and the heat sensor mode can be expressed as

$$R(t) = \frac{3\cos^2\theta(t) - 1}{5} \tag{5}$$

where $R(t)$ is the anisotropy of the heat signal, defined as

$$R(t) = \frac{P_{\parallel}(t) - P_{\perp}(t)}{P_{\parallel}(t) + 2P_{\perp}(t)} \tag{6}$$

where $P_{\parallel}(t)$ and $P_{\perp}(t)$ are the signal intensities from experiments with the detection pulse parallel and perpendicular to the excitation pulse, respectively, and t is the waiting time (T_{w} in Figure 2) between the two pulses.

In general, the heat transfer is not necessarily isotropic. In addition, within the light/matter interaction volume (laser focus spot), the energy source mode and the heat sensor mode do not necessarily have only one relative orientation because molecules to which these modes belong can have various orientations relative to each other. For these cases, eq 5 cannot be immediately applied. Let us consider a simple case: the vibrational cross angle between the two modes has a random value because the molecules are orientated randomly relative to each other. As a result, the heat signal is no longer dependent on the polarizations of laser beams. An identical result from $P_{\parallel}(t)$ and $P_{\perp}(t)$ will be obtained, leading to a zero anisotropic value which gives $\theta = 54.7°$ based on eq 5. The value certainly does not mean that the cross angle between the two modes is 54.7°. In a more general case, a system contains different sets of molecules. In each molecular set, the vibrational cross angle between the energy source mode and the heat sensor mode is a fixed value so that the anisotropy of heat signal from this set of molecules is a single value $R_i(t)$ which contributes to the total signal intensity with a fraction f_i. The total anisotropy is the weighted sum of the individual anisotropies according to the additivity law of anisotropy:[43]

$$R(t) = \sum_i f_i R_i(t) \tag{7}$$

Equation 7 can be derived in the following way. When a system contains different sets of molecules, each with a fixed anisotropy $R_i(t)$ and contributing to the total signal intensity with a fraction f_i, defined as $f_i = P^i(t)/P(t)$, we have

$$R_i(t) = \frac{P_{\parallel}^i(t) - P_{\perp}^i(t)}{P_{\parallel}^i(t) + 2P_{\perp}^i(t)} = \frac{P_{\parallel}^i(t) - P_{\perp}^i(t)}{P_i(t)} \tag{8}$$

where $P_{\parallel}^i(t)$ and $P_{\perp}^i(t)$ are the signal intensities for the ith set of molecules with the detection beam parallel and perpendicular to the excitation beam, respectively, at waiting time t (T_{w}). $P^i(t) = P_{\parallel}^i(t) + 2P_{\perp}^i(t)$ represents the total signal intensity of the ith set of molecules. Thus, we have the total signal intensity $P(t) = P_{\parallel}(t) + 2P_{\perp}(t) = \sum_i P^i(t)$, and $P_{\parallel}(t) = \sum_i P_{\parallel}^i(t)$, $P_{\perp}(t) = \sum_i P_{\perp}^i(t)$.

According to eqs 6 and 8, we obtain

$$\begin{aligned} R(t) &= \frac{P_{\parallel}(t) - P_{\perp}(t)}{P_{\parallel}(t) + 2P_{\perp}(t)} \\ &= \frac{\sum_i P_{\parallel}^i(t) - \sum_i P_{\perp}^i(t)}{P(t)} \\ &= \sum_i \frac{P_{\parallel}^i(t) - P_{\perp}^i(t)}{P^i(t)} \cdot \frac{P^i(t)}{P(t)} \\ &= \sum_i f_i R_i(t) \end{aligned} \tag{9}$$

From the above derivation, we know that f_i is different from the molar fraction of the ith set of molecules in the sample. The two quantities can be considered to be the same only when the three conditions are fulfilled: (1) the distribution of each set of molecules within the light/material interaction is isotropic, (2) their response to the same amount of heat is identical, and (3) the heat transfer rate is isotropic inside each molecular set. The first condition can be easily fulfilled, since experimentally the diameter of interaction cross section is ~100 μm and practically it is not difficult to create a sample with the sizes of randomly distributed microdomains at the order of tens to hundreds of nanometers. The second condition can be problematic for some cases; e.g., in some sets, molecules interact with each other through H-bonds which are highly sensitive to heat effects, and in some sets, because of geometric constraints, the same molecules can only interact with each other through weak intermolecular interactions which are less sensitive to heat effects. The different responses to heat need to be calibrated and normalized for each set of molecules in order to convert the molar fraction into the signal fraction. The third condition is probably fulfilled in most experiments because the number of the low frequency modes (heat) which accept vibrational energy from the energy source mode is large and their transition dipole moment vectors are probably pointing to all directions, resulting in similar heat transfer rates in different directions.

To use eq 7, we assume the signal fraction f_i to be a waiting time independent parameter so that its initial value at time zero can be used. This assumption should hold, since we expect that the lifetimes of the heat modes in different sets of molecules should be very similar within the waiting time period of measurements (tens of ps to several ns) unless there are some molecular transformations occuring during the heat transfer process.

During the waiting time period t (T_{w} in Figure 2), molecules can rotate. If the molecular rotation is fast and the randomization of molecular orientation is completed before heat transfer reaches equilibrium, the anisotropy of heat effects detected will be zero. Therefore, in order to use the heat

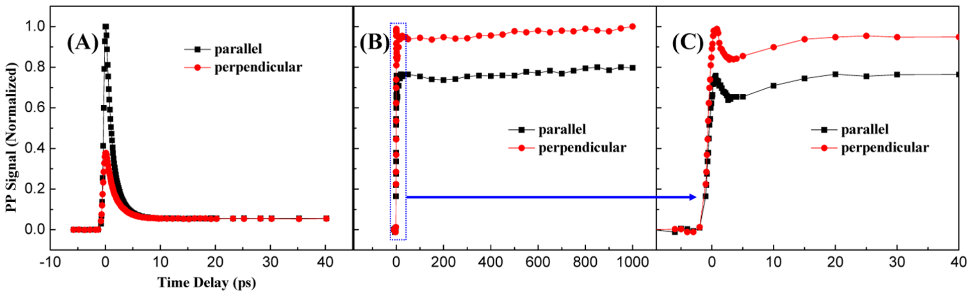

Figure 3. Polarization selective pump/probe data. (A) Pump/probe data of a dilute HOD aqueous solution (1 wt % D_2O in H_2O) with both excitation and detection frequency at 2507 cm^{-1} (OD stretch 0−1 transition frequency). (B) Pump/probe data of a L-cysteine polycrystalline sample with the excitation frequency at 2543 cm^{-1} (SH and NH stretch 0−1 transition frequency) and the detection frequency at 1520 cm^{-1} (NH bending 0−1 transition frequency). (C) Pump/probe data of part B at short waiting times.

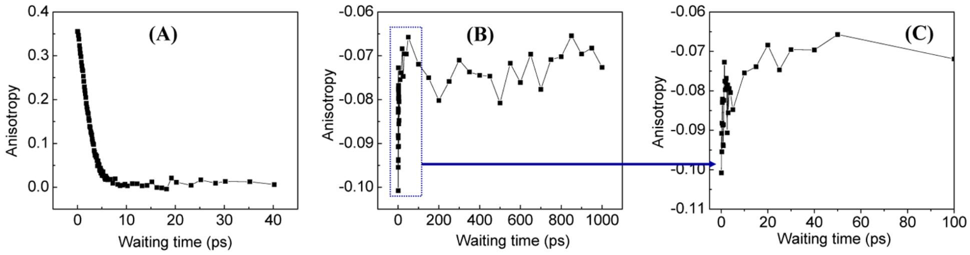

Figure 4. Anisotropies of pump/probe data presented in Figure 3. (A) Waiting time dependent anisotropy data of the HOD aqueous solution; (B and C) waiting time dependent anisotropy data of the L-cysteine crystalline sample.

transfer method to determine relative intermolecular orientations, it is required that the molecular rotational dynamics be independently measured or the molecular rotations are much slower than the heat transfers. Another requirement is that the size of each molecular set or the separations among them should be larger than a certain value. This is because the assumption eq 9 is based on is that the relaxation of the energy source mode can only affect the heat sensor mode within the same molecular set. Modes on other sets will not respond to the relaxation heat of excitation on this molecular set. Each molecular set or their separation needs to be sufficiently large so that most of the relaxation-induced heat only transfers within the same molecular set. We can roughly estimate the critical size which fulfills this requirement. The vibrational lifetime of a high frequency mode in organic molecules is typically a few ps in condensed phases. It takes tens to hundreds of ps for it to convert into heat, which means that after a few hundred ps most signals observed in 2D IR or pump/probe experiments are from heat effects. Now we want to see how big a volume the relaxation-induced heat from a high frequency mode, e.g., 2000 cm^{-1}, can travel at room temperature within a few hundred ps. If the sample density is 1 g/cm^3 with molecular weight 100 g/mol, there are 6.02×10^6 molecules inside a volume of $(100\ nm)^3$. If the heat transfer rate is assumed to be close to the speed of sound in air, e.g., 300 m/s, and the molecular distance is 0.3 nm, it takes about 602 ns for the relaxation-induced heat to travel the volume, $(100\ nm)^3$. Here we assume that the excitation at 2000 cm^{-1} can relax into 10 phonons at room temperature (RT = 200 cm^{-1}). The result indicates that it takes about 600 ps for the phonons to travel a volume of $(10\ nm)^3$. If we want fewer than 15% of the molecules within 5 nm of the surface, the diameter of the volume should be about 200 nm. The estimation given here is very approximate because the actual heat transfer rate can be a few times faster than the value used for the estimation, but it tells us that the critical size is probably at the order of tens to hundreds of nm, dependent on detailed molecular properties. Nonetheless, in the interfacial regions among different molecular sets, the heat signal is randomized, resulting in the measured anisotropy value being smaller than the calculated value from eq 9 without considering the signal randomization in the interfacial region.

Another issue about using eq 5 to determine relative molecular orientations is that the angle determined from eq 5 is the vibrational cross angle which is different from the bond angle needed to determine molecular orientations. As demonstrated before, the vibrational cross angles can be converted into bond angles through quantum molecular calculations with very high precision, which is not heavily dependent on the basis sets of the calculations.[14,16,44]

4. RESULTS AND DISCUSSION

4.1. Anisotropies of Heat Effects in Water and in L-Cysteine Crystal.

The above introduction about the mechanism and signal anisotropy of vibrational relaxation-induced heat effects predicts the following: (1) In a liquid where molecular rotations are faster than the growth of heat effects or molecular orientations are randomized, the signal anisotropy of heat effects is zero. In other words, the pump/probe data of heat effects from both parallel and perpendicular excitation/detection configurations are identical. (2) In a sample where molecular rotations are slow and molecular orientations are anisotropic, the signal anisotropy of heat effects can be nonzero if the energy source mode and the heat sensor mode have a vibrational cross angle other than 54.7°. We used two samples to test this prediction: (1) a 1 wt % D_2O in H_2O liquid sample at room temperature where water molecules rotate with a time constant of ∼2.6 ps and (2) a L-cysteine polycrystalline sample where molecular rotations are almost frozen and molecules are orientated in an ordered anisotropic way of which the crystalline structure has been determined with XRD.[45,46]

Figure 3A displays the polarization selective pump/probe data of the HOD solution with both excitation and detection frequencies at 2507 cm^{-1}, the OD 0−1 transition frequency. At short waiting times, the signal in Figure 3A is from the ground state bleaching of OD stretch because some OD stretch modes have been excited to the first excited state of which the lifetime is 1.3 ps as measured. The bleaching signal begins to decay as the excited modes relax back to the ground state. If there is no heat effect, at a long waiting time (compared to the vibrational lifetime 1.3 ps), e.g., 10 ps, the signal will go to zero. However, as shown, the signal in Figure 1A does not go to zero but remains at an almost constant value at long waiting times. This nonzero signal at long waiting times is caused by the heat effect of which the generation mechanism is exactly the same as that elaborated in the previous section to describe the heat-induced bleaching signal in Figure 1 in the frequency range 2400−2550 cm^{-1}. In Figure 3A, at a long waiting time, e.g., 20 ps, it is obvious that the heat signals from both parallel configurations are identical within experimental uncertainty. The anisotropy of the heat signal remains zero at long waiting times, as shown in Figure 4A. This result is consistent with the first prediction, because the molecular rotational time 2.6 ps is much shorter than the waiting time so that the relative molecular orientations have been randomized.

Very different from the water sample, heat signals in the L-cysteine polycrystalline sample from the two different polarization configurations are not the same. The heat signal from the perpendicular configuration remains constantly larger than that from the parallel configuration at long waiting times, as shown in Figure 3B and C. Figure 3B and C are the polarization selective pump/probe data of the L-cysteine polycrystalline sample by exciting the SH stretch mode at 2543 cm^{-1} (the SH stretch 0−1 transition frequency) which slightly overlaps with the tail of the NH stretch in frequency, and detecting the NH bending mode at 1520 cm^{-1} (the NH bending 0−1 transition frequency). At short waiting times, e.g., 0 ps, the pump/probe signal comes from the ground state bleaching of the vibrational coupling between the SH (+NH stretch because of the frequency overlap) stretch and the NH bending. The signal intensity is dependent on the vibrational cross angle of the two modes, and decays with the lifetime of the SH (+NH) stretches which is measured to be 1.4 ps, as we can see from Figure 3C that a fast decay occurs within a few ps. At longer times, similar to that discussed above, the vibrational relaxation of the first excited states of SH (+NH) stretches produces heat which creates a bleaching signal at the NH bending 0−1 transition frequency as detected. The heat signal is long-lived. Up to 1000 ps, no clear decay is observed (Figure 3B). In addition, the difference between heat signals from the two polarization configurations is remarkable, indicating a nonzero anisotropy value, as shown in Figure 4B and C. The result verifies the above second prediction that the heat signal can be anisotropic if the molecular orientations are anisotropic and molecular rotations are slow.

4.2. Anisotropies of Heat Effects in Glassy and Polycrystalline Polystyrene Samples.

4.2.1. Molecular Conformations and Structures. To further confirm that the nonzero anisotropy of heat signal observed in the crystalline L-cysteine is caused by the anisotropic intermolecular orientations in the solid rather than purely by it being a solid, and to demonstrate that the nonzero anisotropy of heat signal can be quantitatively derived from the relative intermolecular orientations, we further designed experiments to investigate the relaxation-induced heat effects in three solid samples from the same kind of molecules with different intermolecular orientations. Molecules used for this purpose are atactic and syndiotactic polystyrenes. Molecular structures of these two polystyrenes are shown in Figure 5. Polystyrene is a vinyl polymer, which has a long hydrocarbon backbone chain with a phenyl group attached to every other carbon atom. In the syndiotactic polystyrene, the phenyl groups on the polymer chain are attached to alternating sides of the polymer backbone. In the atactic polystyrene, the sides of backbone to which the phenyl groups are attached are disordered. Because of the intrinsic difference in molecular structures, the two polystyrenes adopt different packing patterns when they form solids from melts or solutions. At room temperature, the atactic polystyrene forms amorphous glass because its irregular molecular structure prevents it from forming ordered intermolecular patterns. The molecular chains inside the glass are isotropically distributed.[47] A different situation occurs for the syndiotactic polystyrene. Its regular molecular structure allows it to adopt ordered molecular packing patterns to form crystals at room temperature. Dependent on experimental conditions, syndiotactic polystyrene can form a pure glass or semicrystalline solids with various crystalline structures.[38,48−51]

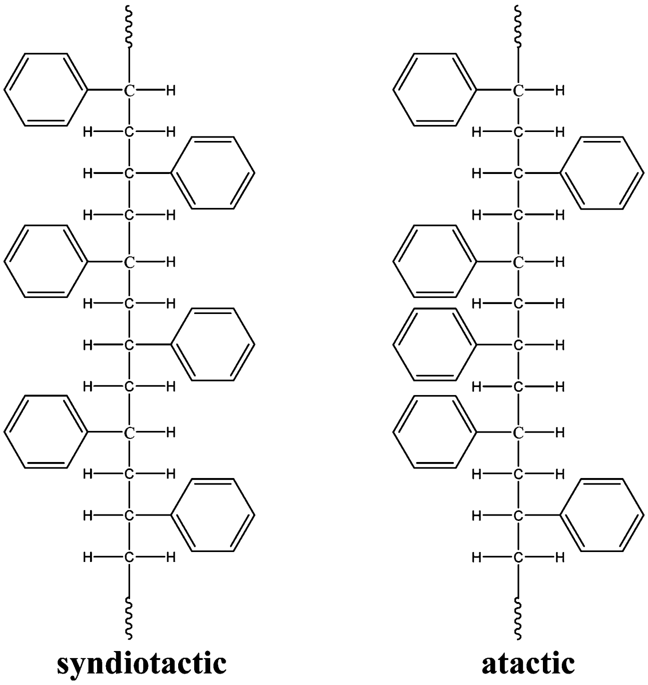

Figure 5. Molecular structures of syndiotactic and atactic polystyrenes.

For our experiments, we prepared three samples with different intermolecular packing patterns: (A) sample 1 is an amorphous glass from the atactic polystyrene, (B) sample 2 is also an amorphous glass from the syndiotactic polystyrene, and (C) sample 3 is a semicrystalline solid containing ~52% of β' crystals and ~48% amorphous glass from the syndiotactic polystyrene. XRD data of the three samples are shown in Figure 6A. There are no clear diffraction peaks (black and red curves in Figure 6A) in samples 1 and 2, indicating that molecular distributions inside the samples are random. Sample 3 has clear diffraction peaks (the blue curve in Figure 6A), indicating that

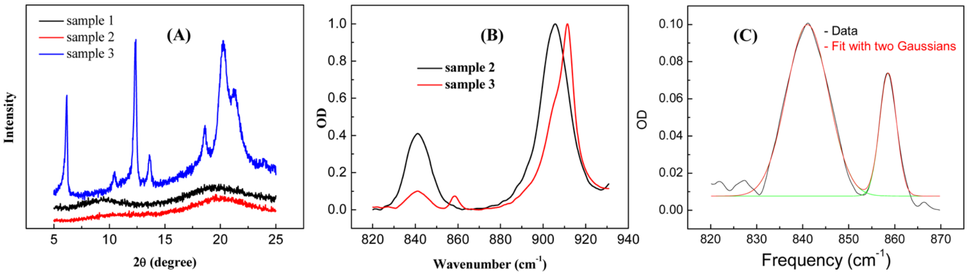

Figure 6. (A) XRD data of the three polystyrene samples. Only sample 3 shows clearly diffraction peaks. Samples 1 and 2 only have two very broad bumps, indicating they are mostly amorphous. (B) FTIR data of samples 2 and 3 at room temperature. Peaks at around 905 and 841 cm^{-1} are characteristic for the amorphous domains of the syndiotactic polystyrene, and the two peaks at 911 and 858 cm^{-1} belong to the β' crystal of the syndiotactic polystyrene.[53,54] (C) FTIR spectrum of sample 3 and the peak fitting result with two Gaussians.

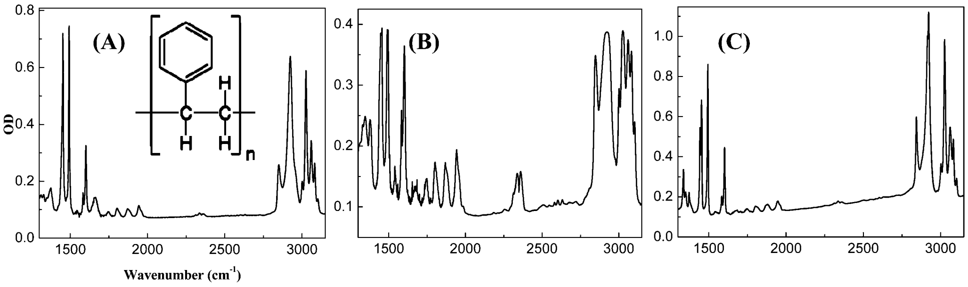

Figure 7. FTIR spectra of (A) sample 1, (B) sample 2, and (C) sample 3. Inset: molecular formula of polystyrene. The assignments for peaks involved in the relaxation heat-induced measurements are ring CC stretch (1600 cm^{-1}), backbone CH_2 stretch (2924 cm^{-1}), and ring CH stretch (3026 cm^{-1}, 3060 cm^{-1}).

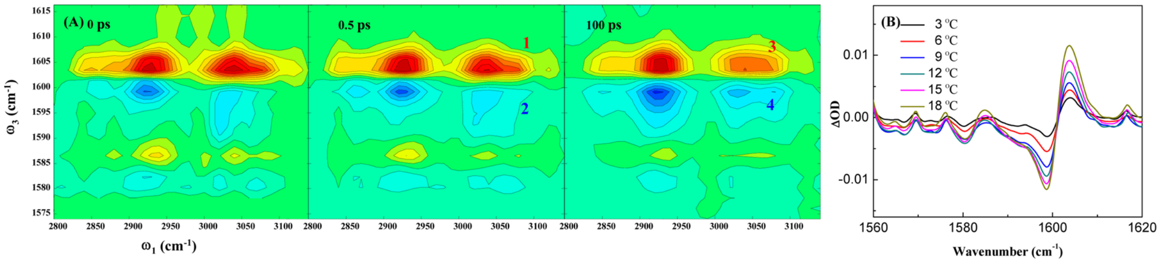

Figure 8. (A) 2D IR spectra of sample 3 at different waiting times. Each contour represents 10% intensity change. (B) Temperature difference FTIR spectra of sample 3 obtained by subtracting the FTIR spectrum at a higher temperature from the spectrum at room temperature (21 °C); e.g., line 3 °C represents the subtraction result from 21 to 24 °C.

periodical ordered molecular patterns exist in the sample. By comparing the XRD data in Figure 6A to the literature, we found that the crystalline structure of sample 3 is the so-called "β' crystal".[50,52] Typically, it is very difficult for a polymer sample to 100% form crystalline structures because during the crystallization process there are always some polymer chains which are entangled and form amorphous domains. The crystalline content (crystallinity) of a polymer sample varies with crystallization conditions. To determine the crystallinity of sample 3, we use FTIR data (Figure 6B) instead of XRD data (Figure 6A) because the XRD method is not sensitive to the amorphous domains. According to the literature,[53,54] peaks at around 905 and 841 cm^{-1} are characteristic for the amorphous domains of the syndiotactic polystyrene, and the two peaks at 911 and 858 cm^{-1} belong to its β' crystal. In the FTIR spectrum of sample 3 in Figure 6B (the red curve), all four peaks exist, indicating that both amorphous domains and β' crystalline domains coexist in the sample. The molar ratio of these two domains can be determined by the normalized area ratio of the two peaks at 841 cm^{-1} (amorphous) and 858 cm^{-1} (β'). According to the literature,[53,54] the extinction coefficient ratio α of peak 858 cm^{-1} over peak 841 cm^{-1} is 0.272. Therefore, the crystallinity of β' crystalline domains in sample 3 is

$$c = \left(\frac{A_{858}}{\alpha}\right) \Big/ \left(\frac{A_{858}}{\alpha} + A_{841}\right) \tag{10}$$

where A_{858} and A_{841} are the areas of the peaks at 858 and 841 cm^{-1}, respectively. Experimentally, the two areas were determined to be 0.31 and 1.05, respectively, by fitting the peaks with two Gaussians (Figure 6C). On the basis of these values and eq 10, the crystallinity in sample 3 is determined to be 52%. The value is slightly higher than 38.3% determined on the basis of the same method on a crystal prepared under a similar condition.[53,54] A very possible reason for this difference is that the polymer we used is from a different company. Its molecular weight and quality of structural regularity which can affect crystallization can be different from the one used in the literature.

4.2.2. 1D and 2D IR Data. The major FTIR spectral features of the three samples in Figure 7 (A, sample 1; B, sample 2; C,

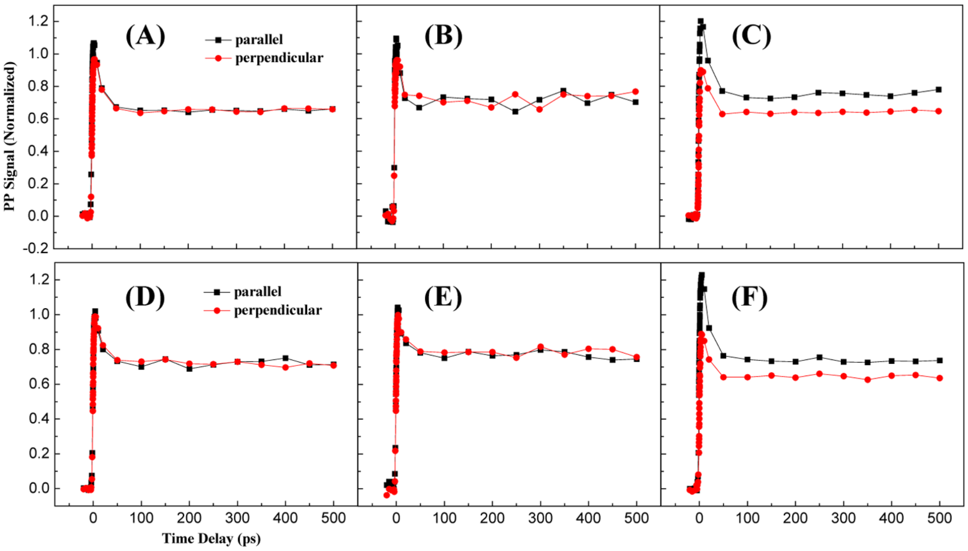

Figure 9. Time dependent polarization selective intensities of peaks at ω_1 = 3060 cm^{-1} and ω_3 = 1600 cm^{-1} of (A) sample 1, (B) sample 2, and (C) sample 3, respectively, and polarization selective time dependent intensities of peaks at ω_1 = 2924 cm^{-1} and ω_3 = 1600 cm^{-1} of (D) sample 1, (E) sample 2, and (F) sample 3, respectively. Each set of the data was normalized according to the initial maximum of the total intensity $P(t)$.

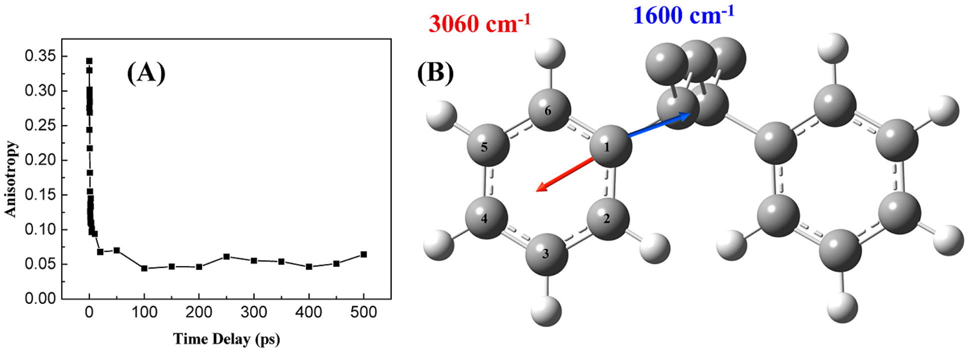

Figure 10. (A) The time dependent anisotropy of sample 3 calculated from Figure 9C. The initial value 0.35 indicates that the directions of the excitational mode and the detection mode are nearly parallel to each other. (B) The transition dipole moment directions of the ring CH stretch (3060 cm^{-1}) and the ring CC stretch (1600 cm^{-1}) modes within a benzene ring. In the figure, the backbone of polystyrene is pointing along the paper normal.

sample 3) are very similar. All of them contain the following peaks investigated in the vibrational relaxation induced-heat measurements: the ring CC stretch (1600 cm^{-1}), the ring CH stretch (3026 cm^{-1}, 3060 cm^{-1}), and the backbone CH$_2$ stretch (2924 cm^{-1}). The first three modes are delocalized within the benzene ring. In 2D IR measurements, the absorption changes of the ring CC stretch peak (1600 cm^{-1}) were recorded as a function of waiting time after the respective excitation of the other three modes.

Figure 8A shows waiting time dependent 2D IR spectra of sample 3. At earlier waiting times, e.g., 0 and 0.5 ps, similar to those in Figure 1, the peaks in Figure 8A are mainly contributed by vibrational couplings between chain CH$_2$ stretch mode (2924 cm^{-1}) or ring CH stretch mode (3026 cm^{-1}, 3060 cm^{-1}) and ring CC stretch mode (1600 cm^{-1}). At a relatively long waiting time, e.g., 100 ps, the peaks in the 2D IR spectra are mainly from the vibrational relaxation−induced heat effects, as the vibrational lifetimes of the CH stretches are only ∼2 ps. The heat signal is not significantly different from the coupling signal in Figure 8A. Only the lineshapes slightly change. The optical absorbance changes caused by relaxation-induced heat are consistent with the temperature difference FTIR spectra shown in Figure 8B.

The time dependent polarization selective intensities of peaks at ω_1 = 3060 cm^{-1}, ω_1= 2924 cm^{-1}, and ω_3 = 1600 cm^{-1} of the three samples are shown in Figure 9. In samples 1 (Figure 9A and D) and 2 (Figure 9B and E), signals from both parallel and perpendicular polarization configurations become equal regardless of whether the initial vibrational coupling signals at time 0 are the same or not. As discussed above, the results are expected, since these two samples are amorphous glass. Inside the two samples, the relative intermolecular orientations are random, resulting in isotropic vibrational relaxation-induced heat signals at long waiting times. For sample 3 inside which a good portion of molecules form crystals, the heat signals from the two polarization configurations are not equal anymore, as shown in Figure 9C and F. The signals from the parallel polarization configuration remain constantly larger than those from the perpendicular configuration after 100 ps. There is one point we need to emphasize here. The heat effects observed in the samples are mainly from the intermolecular rather than intramolecular heat transfer accompanying the vibrational relaxation of the initially excited

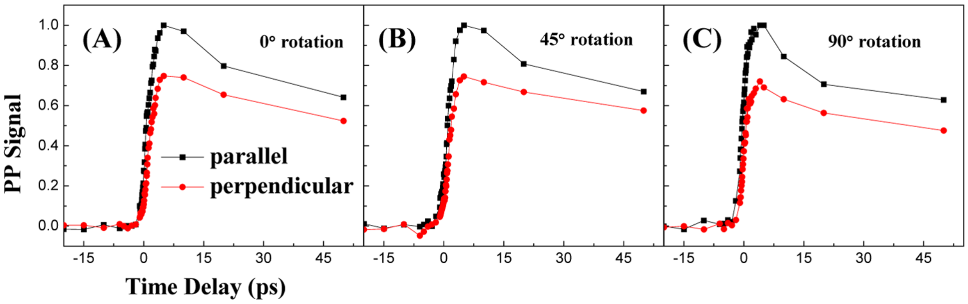

Figure 11. Time dependent polarization selective intensities of peaks with ω_1 = 3060 cm^{-1} and ω_3 = 1600 cm^{-1} of sample 3 at three different sample orientations. A similar intensity ratio between the two polarization configurations at all three sample orientations indicates that the molecular distribution within the laser focus spot is isotropic.

mode. This conclusion is supported by a control experiment: the heat effect by exciting/detecting the same pair of modes in a 2 wt % polystyrene/chloroform solution is significantly smaller than that in the bulk polystyrene solid sample because most of the heat (~85% as measured) is transferred to the solvent chloroform molecules. Data are shown in the Supporting Information.

4.2.3. Anisotropy of Heat Effects and Molecular Orientations of Sample 3. The time dependent anisotropy of pump/probe signal of sample 3 in Figure 9C was calculated on the basis of eq 6 and shown in Figure 10A. The initial anisotropic value can be used to determine the intramolecular vibrational cross angle between the initially excited vibrational mode, the ring CH stretch (3060 cm^{-1}), and the detection mode, the ring CC stretch (1600 cm^{-1}), provided that the molecular distribution within the matter/light interaction volume is isotropic.[15] To test whether the molecular orientation in sample 3 is random within the laser focus spot, we rotated the sample 45 and 90° in addition to 0° to acquire data. There is a similar intensity ratio between the two polarization configurations at all three sample orientations (0, 45, and 90°, relative to the optical table plane), indicating a macroscopic random molecular distribution within the laser focus spot. Results are displayed in Figure 11 (A, 0°; B, 45°; C, 90°).

The initial anisotropic value in Figure 10A is 0.35, which indicates that the vibrational cross angle between the excitation and detection modes (the ring CH stretch (3060 cm^{-1}) and the ring CC stretch (1600 cm^{-1})) is ~17° according to eq 5. This is consistent with our density functional theory (DFT) calculations. The calculated directions of these two vibrational modes are nearly parallel (~8.6°) to each other within a benzene ring, both of which are along the C(1)−C(4) axis within the benzene ring, as shown in Figure 10B. In this sample, the vibrational coupling between these two modes on different rings is too weak to be detected because of the large distance between two rings. Therefore, the calculated cross angle between these two modes on different rings is not taken into consideration. The DFT calculation details are provided in the Supporting Information.

Figure 10A shows that the anisotropy decays rapidly after the initial vibrational excitation. Within about 10 ps, the anisotropy value drops from ~0.35 to ~0.1, and at longer times, it essentially remains constant at 0.05 ± 0.01. In sample 3, the polymer molecules are in either the glassy state or the crystalline state. Their rotations are expected to be hindered and extremely slow. Therefore, the initial fast anisotropy observed should not be caused by the molecular rotations. The resonant vibrational energy transfer among the initial excitational modes (the ring CH stretch at 3060 cm^{-1}) on different benzene rings is not a likely reason either, because their transition dipole moment is too small and their relative distances are too large to effectively transfer energy to each other within a few ps, compared to the KSCN systems we studied previously.[20,21] The most likely reason for the initial fast anisotropy decay is the vibrational relaxation-induced heat effects. As measured, the vibrational lifetime of the CH stretch is only 2.1 ps. Its relaxation within the initial few ps produces a significant amount of heat which dissipates intramolecularly into other segments of the same polymer chain and intermolecularly into other molecules. At early waiting times when the amount of vibrational relaxation is small, the anisotropy of the signal in Figure 10A is determined by the cross angle between the ring CH stretch mode and the ring CC stretch mode which is purely determined by the intraring atomic positions, since both modes are on the same ring. At longer waiting times when relaxation-induced heat effects become significant, the detection mode, the ring CC stretch, is not necessarily on the same ring as the initial excited mode, the ring CH stretch, because the same mode on different rings experiences the same heat and optically responds similarly to the heat as it dissipates away from the initially excited ring. Therefore, the anisotropy value under this circumstance is determined by the average angle between the two modes on both the same and different rings. As discussed above, sample 3 has ~48% amorphous domains which give an anisotropy value of 0. In the rest of the 52% crystalline domains, the relative orientations of benzene rings are not parallel, which can also reduce the anisotropy from the initial value 0.35, since 0.35 is close to the possible maximum anisotropy value 0.4 from a pair of parallel modes. Therefore, because of the intermolecular and inter-ring relative orientations, no matter in the glass domains or the crystalline domains, the heat effects reduce the anisotropy value. However, before the majority of the initial excitation of the ring CH stretch has relaxed, the anisotropy value of the signal in Figure 10A contains contributions from vibrational couplings, possible mode specific vibrational energy transfers, and the heat effects. It would be very complicated to extract the relative intermolecular orientations in sample 3 from the mixed signals which come from at least three different mechanisms. At longer waiting times, e.g., after 100 ps, most of the initial excitation of the ring CH stretch has relaxed into heat, as indicated by the time independent heat signals in Figure 9C. The pump/probe signals observed in Figure 9C are mainly from the heat effects. Now it is possible to analyze the intermolecular orientations in sample 3 based on the anisotropy

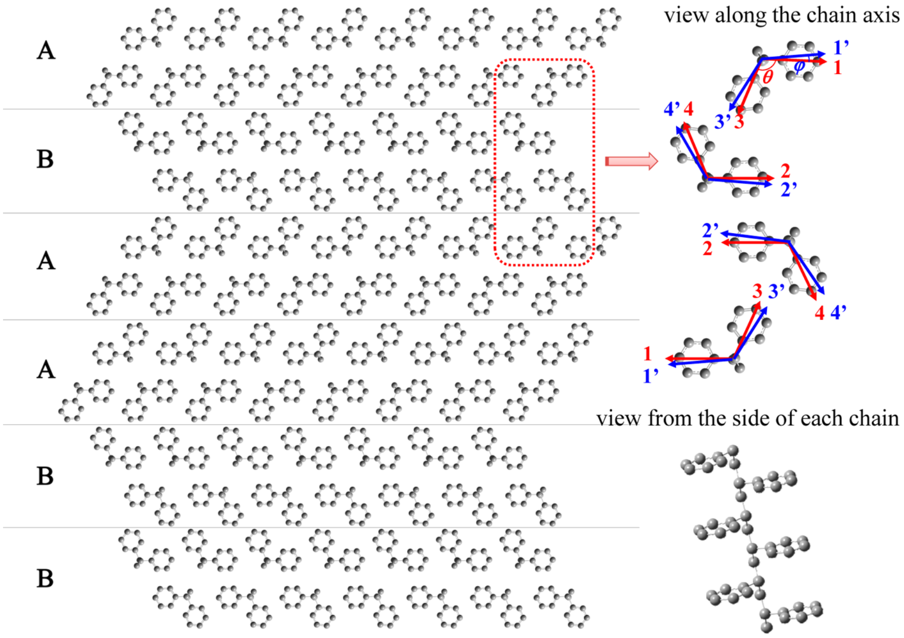

Figure 12. Stacking of macromolecular bilayers in the β' crystal, with A and B indicating two kinds of macromolecular bilayers.[52] The upper right represents the chains of four different orientations, with red and blue arrows indicating the transition dipole moment directions of the ring CH stretch (3060 cm^{-1}) and the ring CC stretch (1600 cm^{-1}) modes, respectively. The bottom right shows the molecular conformation of a polymer chain.

value at long waiting times in Figure 10A, according to the equations given in section 3.

According to eq 9, the total anisotropy of heat signal is the weighed sum of subcomponents' anisotropies. In sample 3, there are two components: (1) the amorphous glass of which the anisotropy is 0 and (2) the ordered crystals of which the anisotropy is dependent on the molecular orientations and inter-ring orientations within a polymer chain. The molar fractions of these two domains are 48% (glass) and 52% (crystal), respectively. However, as discussed in section 3, the molecular fraction can be used as the weighing factor in eq 9 only when the three conditions are simultaneously fulfilled. For sample 3, we found that it fit the criteria: (1) The molecular distribution within the light/material interaction is isotropic, as supported by the observed same anisotropic behaviors obtained by rotating the sample. (2) The molecular responses in different domains are approximately identical (±10%), as we can see from the normalized intensities of heat signals in Figure 9C compared to those in Figure 9A or B. (3) The results in (2) also indicate the heat transfer inside the crystal is probably isotropic, since the heat transfers are very similar in both amorphous and crystalline states. As discussed in section 3, the dimensions of the crystalline and amorphous domains must be larger than tens of nm in order for most of the relaxation-induced heat to travel within the same domains. We do not have direct evidence to show how large the domains are, but from the opaque nature of sample 3, we estimate that at least one dimension of the crystals must be larger than 100 nm (1/4 of 400 nm). The photographs of samples 1 and 3 are provided in the Supporting Information, where the glassy sample 1 is transparent but the semicrystalline sample 3 is opaque.

To calculate the anisotropy of heat signal from the β' crystalline domains of sample 3, we need information about its molecular conformations and crystalline structures. According to the literature,[38,52,55] inside the β' crystalline domains, a polystyrene molecule takes the all-trans-planar-zigzag (T4) chain conformation, as shown in the bottom right of Figure 12. The molecular orientations inside the crystal are also displayed in the left side of Figure 12. When viewed along the chain axis, the crystal can be described in terms of a slightly disordered stacking of two kinds of macromolecular bilayers characterized by different orientations of lines connecting two adjacent benzene rings inside each chain, indicated as A and B in Figure 12. As a result of crystalline symmetry, the benzene rings can be divided into four groups according to the different orientations to calculate the anisotropy value, with the molar fraction of 1:1:1:1. As shown in the upper right of Figure 12, the different transition dipole moment directions of the energy source mode, the ring CH stretch (3060 cm^{-1}) and the heat sensor mode, the ring CC stretch (1600 cm^{-1}) are denoted as direction 1−4 and 1′−4′, respectively. φ is the vibrational cross angle between the two modes within the same ring, which is 8.6° from DFT calculation. θ is the cross angle between the energy source modes in two different directions within a single chain. As shown in Figure 10B, the calculated directions of the energy source mode are along the C(1)−C(4) axis. Therefore, according to the crystal structure,[52] the cross angle θ can be obtained as 111°. Here we take both the CH and CC stretch transition dipole moment vectors to be within the ring plane to simplify calculations. This can cause about 1−5% uncertainty in the final result, since the calculated CC stretch has a cross angle of 2−3° out of the benzene plane.

The energy source modes in four different directions 1−4 has an equal probability to be excited, and hence contribute equally to the total anisotropy of the crystalline region from each direction. For the energy source modes at direction 1, the heat sensor modes can be divided into four species according to different directions 1′−4′, with the cross angle between the energy source mode and the heat sensor modes as φ, φ, $\theta + \varphi$, and $\theta + \varphi$, successively. Then, the corresponding anisotropy can be calculated from

$$R_1 = \frac{1}{4}\cdot\left(\frac{3\cos^2\varphi - 1}{5} + \frac{3\cos^2\varphi - 1}{5} + \frac{3\cos^2(\theta+\varphi) - 1}{5} + \frac{3\cos^2(\theta+\varphi) - 1}{5}\right) = 0.3\cdot(\cos^2\varphi + \cos^2(\theta+\varphi)) - 0.2 \quad (11)$$

In the same manner, the anisotropic value for the other three situations, i.e., the energy source mode at direction 2, 3, or 4, can be therefore obtained from

$$R_2 = \frac{1}{4}\cdot\left(\frac{3\cos^2\varphi - 1}{5} + \frac{3\cos^2\varphi - 1}{5} + \frac{3\cos^2(\theta+\varphi) - 1}{5} + \frac{3\cos^2(\theta+\varphi) - 1}{5}\right) = 0.3\cdot(\cos^2\varphi + \cos^2(\theta+\varphi)) - 0.2 \quad (12)$$

$$R_3 = \frac{1}{4}\cdot\left(\frac{3\cos^2(\theta+\varphi) - 1}{5} + \frac{3\cos^2(\theta-\varphi) - 1}{5} + \frac{3\cos^2(\varphi) - 1}{5} + \frac{3\cos^2(2\theta+\varphi) - 1}{5}\right) = 0.15\cdot(\cos^2(\theta+\varphi) + \cos^2(\theta-\varphi) + \cos^2\varphi + \cos^2(2\theta+\varphi)) - 0.2 \quad (13)$$

and

$$R_4 = \frac{1}{4}\cdot\left(\frac{3\cos^2(\theta-\varphi) - 1}{5} + \frac{3\cos^2(\theta+\varphi) - 1}{5} + \frac{3\cos^2(2\theta+\varphi) - 1}{5} + \frac{3\cos^2(\varphi) - 1}{5}\right) = 0.15\cdot(\cos^2(\theta-\varphi) + \cos^2(\theta+\varphi) + \cos^2(2\theta+\varphi) + \cos^2\varphi) - 0.2 \quad (14)$$

where the four terms in each bracket represent the contribution from the heat sensor mode in directions 1′–4′, respectively. Then, the total anisotropy in the crystal region can be calculated by substituting the angles $\theta = 111°$ and $\varphi = 8.6°$:

$$R_\beta = \frac{1}{4}(R_1 + R_2 + R_3 + R_4) = 0.075\cdot(3\cos^2\varphi + 3\cos^2(\theta+\varphi) + \cos^2(\theta-\varphi) + \cos^2(2\theta+\varphi)) - 0.2 \approx 0.109 \quad (15)$$

As discussed above, the overall anisotropy of sample 3 should be a weighted average of two components, i.e., crystalline and amorphous regions, which can be obtained according to eq 7. The fraction f_i here can be replaced by the molar fraction of each set of molecules in different regions for the reasons we have discussed. Above all, we can finally get

$$R_{\text{total}} = c\cdot 0.109 + (1 - c)\cdot 0 \quad (16)$$

with c representing the molar fraction of molecules in the crystalline region and R_{total} is the total anisotropy. With $c = 52\%$ obtained from FTIR spectra described above, calculation from eq 16 gives $R_{\text{total}} = 0.057$. The value is identical to $R_{\text{measured}} = 0.05 \pm 0.01$ experimentally measured. If we treat c as an unknown parameter with $R_{\text{total}} = R_{\text{measured}} = 0.05 \pm 0.01$, we obtain $c = 46 \pm 9\%$. This value is consistent with 52% calculated from FTIR spectra. The result also indicates that within 500 ps the induced heat from the relaxation of ring CH stretch excitation mainly travels inside each crystalline or amorphous domain where the originally excited mode resides.

There can be one concern about the method presented here: the calculated cross angle between two vibrational modes is for a molecule with all vibrational modes at the ground state. If the heat effects could significantly change the cross angle, the result from the method would be meaningless. This issue can be experimentally examined, and in practice, it is not a concern at all. According to the Feynman diagrams in Figure 2, the red peak 3 in Figure 8A of which the intensities are used in the above analysis is from the 0−1 transition of the sensor mode (the ring CC stretch) under the condition that those low frequency modes are not excited, and the blue peak 4 underneath is from the 0−1 transition of the sensor mode under the condition that the low frequency modes are excited by the relaxation. Comparing the anisotropy values from both red and blue peaks can immediately tell us whether the heat effects can change the cross angle or not. For this particular system, both peaks 3 and 4 give the same anisotropy value of ~0.05 at long waiting times (data are provided in the Supporting Information), indicating that the cross angle is not changed by the heat effects. This is consistent with our previous results about the effect of combination band excitation on the vibrational cross angles in two other systems.[14−16] In practice, to be safe, using data from the red peaks can completely avoid this problem.

5. CONCLUDING REMARKS

In this work, through investigating a series of liquid, glassy, and crystalline samples, we demonstrated that the signal anisotropy of vibrational relaxation-induced heat effects is determined by both relative molecular orientations and rotations. If the relative molecular orientations are randomized or molecular rotations are fast compared to heat transfer, the signal anisotropy of heat effects is zero. If the relative molecular orientations are anisotropic and the molecular rotations are slow, the signal anisotropy of heat effects can be nonzero, which is determined by the relative orientations of the energy source mode and the heat sensor mode within the same molecule and in different molecules. We also demonstrated that the correlation between the anisotropy value of heat signal and the relative molecular orientation can be quantitatively calculated.

The samples used to demonstrate the nonzero anisotropy of heat signal are crystalline. Here we want to emphasize that the method should not be limited for crystalline samples. Only if the molecular rotations are slow and the separations among different energy source/heat sensor pairs are sufficiently large, the nonzero anisotropy value of heat signal should be applicable to analyze the relative orientation between the energy source molecule and the heat sensor molecule.

In this work, we only demonstrated that the nonzero anisotropy of heat signal can be calculated from relative molecular orientations. In principle, it should work in the reverse order. In other words, it should be possible to derive the relative molecular orientations from nonzero anisotropy values if a sufficient number of different energy source/heat sensor pairs are measured. This is subject to our future work. In addition, in this work, we only qualitatively discuss that the sizes of molecular domains can affect the anisotropy values. Future experiments are needed to quantitatively address this issue.

■ ASSOCIATED CONTENT

Ⓢ Supporting Information

Supporting figures and data about DFT calculations, anisotropy measurements, and sample pictures. This material is available free of charge via the Internet at http://pubs.acs.org.

■ AUTHOR INFORMATION

Corresponding Author

*Phone: 001-713-348-2048. E-mail: junrong@rice.edu.

Notes

The authors declare no competing financial interest.

■ ACKNOWLEDGMENTS

This material is based upon work supported by the Air Force Office of Scientific Research under AFOSR Award No. FA9550-11-1-0070 and the Welch foundation under Award No. C-1752. J.R.Z. also thanks the David and Lucile Packard Foundation for a Packard fellowship. Idemitsu Kosan Co. Ltd, Japan, is highly appreciated for providing free sPS materials. We also thank Prof. Robert F. Curl for reading the manuscript and insightful suggestions.

■ REFERENCES

(1) DeFlores, L. P.; Ganim, Z.; Nicodemus, R. A.; Tokmakoff, A. Amide I′-II′ 2D IR Spectroscopy Provides Enhanced Protein Secondary Structural Sensitivity. *J. Am. Chem. Soc.* **2009**, *131*, 3385−3391.

(2) Finkelstein, I. J.; Zheng, J. R.; Ishikawa, H.; Kim, S.; Kwak, K.; Fayer, M. D. Probing Dynamics of Complex Molecular Systems with Ultrafast 2D IR Vibrational Echo Spectroscopy. *Phys. Chem. Chem. Phys.* **2007**, *9*, 1533−1549.

(3) Ernst, R. R.; Bodenhausen, G.; Wokaun, A. *Nuclear Magnetic Resonance in One and Two Dimensions*; Oxford University Press: Oxford, U.K., 1987.

(4) Khalil, M.; Demirdoven, N.; Tokmakoff, A. Coherent 2D IR Spectroscopy: Molecular Structure and Dynamics in Solution. *J. Phys. Chem. A* **2003**, *107*, 5258−5279.

(5) Bredenbeck, J.; Helbing, J.; Hamm, P. Labeling Vibrations by Light: Ultrafast Transient 2D-IR Spectroscopy Tracks Vibrational Modes during Photoinduced Charge Transfer. *J. Am. Chem. Soc.* **2004**, *126*, 990−991.

(6) Shim, S. H.; Strasfeld, D. B.; Ling, Y. L.; Zanni, M. T. Automated 2D IR Spectroscopy Using a Mid-IR Pulse Shaper and Application of This Technology to the Human Islet Amyloid Polypeptide. *Proc. Natl. Acad. Sci. U.S.A.* **2007**, *104*, 14197−14202.

(7) Baiz, C. R.; Nee, M. J.; McCanne, R.; Kubarych, K. J. Ultrafast Nonequilibrium Fourier-Transform Two-Dimensional Infrared Spectroscopy. *Opt. Lett.* **2008**, *33*, 2533−2535.

(8) Rubtsov, I. V.; Kumar, K.; Hochstrasser, R. M. Dual-Frequency 2D IR Photon Echo of a Hydrogen Bond. *Chem. Phys. Lett.* **2005**, *402*, 439−443.

(9) Maekawa, H.; Formaggio, F.; Toniolo, C.; Ge, N. H. Onset of 3(10)-Helical Secondary Structure in aib Oligopeptides Probed by Coherent 2D IR Spectroscopy. *J. Am. Chem. Soc.* **2008**, *130*, 6556−6566.

(10) Cowan, M. L.; Bruner, B. D.; Huse, N.; Dwyer, J. R.; Chugh, B.; Nibbering, E. T. J.; Elsaesser, T.; Miller, R. J. D. Ultrafast Memory Loss and Energy Redistribution in the Hydrogen Bond Network of Liquid H2O. *Nature* **2005**, *434*, 199−202.

(11) Zheng, J.; Kwak, K.; Asbury, J. B.; Chen, X.; Piletic, I.; Fayer, M. D. Ultrafast Dynamics of Solute-Solvent Complexation Observed at Thermal Equilibrium in Real Time. *Science* **2005**, *309*, 1338−1343.

(12) Zheng, J.; Kwac, K.; Xie, J.; Fayer, M. D. Ultrafast Carbon-Carbon Single Bond Rotational Isomerization in Room Temperature Solution. *Science* **2006**, *313*, 1951−1955.

(13) Bredenbeck, J.; Ghosh, A.; Smits, M.; Bonn, M. Ultrafast Two Dimensional-Infrared Spectroscopy of a Molecular Monolayer. *J. Am. Chem. Soc.* **2008**, *130*, 2152−2153.

(14) Bian, H.; Li, J.; Wen, X.; Sun, Z.; Song, J.; Zhuang, W.; Zheng, J. Mapping Molecular Conformations with Multiple-Mode Two-Dimensional Infrared Spectroscopy. *J. Phys. Chem. A* **2011**, *115*, 3357−3365.

(15) Chen, H.; Bian, H.; Li, J.; Wen, X.; Zheng, J. Ultrafast Multiple-Mode Multiple-Dimensional Vibrational Spectroscopy. *Int. Rev. Phys. Chem.* **2012**, *31*, 469−565.

(16) Bian, H.; Li, J.; Chen, H.; Yuan, K.; Wen, X.; Li, Y.; Sun, Z.; Zheng, J. Molecular Conformations and Dynamics on Surfaces of Gold Nanoparticles Probed with Multiple-Mode Multiple-Dimensional Infrared Spectroscopy. *J. Phys. Chem. C* **2012**, *116*, 7913−7924.

(17) Bian, H.; Li, J.; Wen, X.; Zheng, J. R. Mode-Specific Intermolecular Vibrational Energy Transfer: 1. Phenyl Selenocyanate and Deuterated Chloroform Mixture. *J. Chem. Phys.* **2010**, *132*, 184505.

(18) Bian, H. T.; Wen, X. W.; Li, J. B.; Zheng, J. R. Mode-Specific Intermolecular Vibrational Energy Transfer. II. Deuterated Water and Potassium Selenocyanate Mixture. *J. Chem. Phys.* **2010**, *133*, 034505.

(19) Li, J.; Bian, H.; Chen, H.; Wen, X.; Hoang, B.; Zheng, J. Ion Association in Aqueous Solutions Probed through Vibrational Energy Transfers among Cation, Anion and Water Molecules. *J. Phys. Chem. B* **2012**, in press.

(20) Bian, H.; Chen, H.; Li, J.; Wen, X.; Zheng, J. Nonresonant and Resonant Mode-Specific Intermolecular Vibrational Energy Transfers in Electrolyte Aqueous Solutions. *J. Phys. Chem. A* **2011**, *115*, 11657−11664.

(21) Bian, H.; Wen, X.; Li, J.; Chen, H.; Han, S.; Sun, X.; Song, J.; Zhuang, W.; Zheng, J. Ion Clustering in Aqueous Solutions Probed with Vibrational Energy Transfer. *Proc. Natl. Acad. Sci. U.S.A.* **2011**, *108*, 4737.

(22) Li, J. B.; Bian, H. T.; Wen, X. W.; Chen, H. L.; Yuan, K. J.; Zheng, J. R. Probing Ion/Molecule Interactions in Aqueous Solutions with Vibrational Energy Transfer. *J. Phys. Chem. B* **2012**, *116*, 12284−12294.

(23) Bian, H.; Li, J.; Zhang, Q.; Chen, H.; Zhuang, W.; Gao, Y. Q.; Zheng, J. Ion Segregation in Aqueous Solutions. *J. Phys. Chem. B* **2012**, *116*, 14426.

(24) Bian, H. T.; Zhao, W.; Zheng, J. R. Intermolecular Vibrational Energy Exchange Directly Probed with Ultrafast Two Dimensional Infrared Spectroscopy. *J. Chem. Phys.* **2009**, *131*, 124501.

(25) Dlott, D. D. Vibrational Energy Redistribution in Polyatomic Liquids: 3D Infrared-Raman Spectroscopy. *Chem. Phys.* **2001**, *266*, 149−166.

(26) Asbury, J. B.; Steinel, T.; Stromberg, C.; Gaffney, K. J.; Piletic, I. R.; Goun, A.; Fayer, M. D. Hydrogen Bond Dynamics Probed with Ultrafast Infrared Heterodyne Detected Multidimensional Vibrational Stimulated Echoes. *Phys. Rev. Lett.* **2003**, *91*, 237402.

(27) Steinel, T.; Asbury, J. B.; Zheng, J. R.; Fayer, M. D. Watching Hydrogen Bonds Break: A Transient Absorption Study of Water. *J. Phys. Chem. A* **2004**, *108*, 10957−10964.

(28) Kurochkin, D. V.; Naraharisetty, S. R. G.; Rubtsov, I. V. A Relaxation-Assisted 2D IR Spectroscopy Method. *Proc. Natl. Acad. Sci. U.S.A.* **2007**, *104*, 14209−14214.

(29) Rubtsov, I. V. Relaxation-Assisted Two-Dimensional Infrared (RA 2DIR) Method: Accessing Distances over 10 Å and Measuring Bond Connectivity Patterns. *Acc. Chem. Res.* **2009**, *42*, 1385−1394.

(30) Kasyanenko, V. M.; Tesar, S. L.; Rubtsov, G. I.; Burin, A. L.; Rubtsov, I. V. Structure Dependent Energy Transport: Relaxation-Assisted 2DIR Measurements and Theoretical Studies. *J. Phys. Chem. B* **2011**, *115*, 11063−11073.

(31) Wang, Z. H.; Carter, J. A.; Lagutchev, A.; Koh, Y. K.; Seong, N. H.; Cahill, D. G.; Dlott, D. D. Ultrafast Flash Thermal Conductance of Molecular Chains. *Science* **2007**, *317*, 787−790.

(32) Dai, J.; Xie, X.; Zhang, X. C. Detection of Broadband Terahertz Waves with a Laser-Induced Plasma in Gases. *Phys. Rev. Lett.* **2006**, *97*, 103903.

(33) Xie, X.; Dai, J.; Zhang, X. C. Coherent Control of THz Wave Generation in Ambient Air. *Phys. Rev. Lett.* **2006**, *96*, 075005.

(34) Cheng, M.; Reynolds, A.; Widgren, H.; Khalil, M. Generation of Tunable Octave-Spanning Mid-Infrared Pulses by Filamentation in Gas Media. *Opt. Lett.* **2012**, *37*, 1787−1789.

(35) Baiz, C. R.; Kubarych, K. J. Ultrabroadband Detection of a Mid-IR Continuum by Chirped-Pulse Upconversion. *Opt. Lett.* **2011**, *36*, 187−189.

(36) Petersen, P. B.; Tokmakoff, A. Source for Ultrafast Continuum Infrared and Terahertz Radiation. *Opt. Lett.* **2010**, *35*, 1962−1964.

(37) Calabrese, C.; Stingel, A. M.; Shen, L.; Petersen, P. B. Ultrafast Continuum Mid-Infrared Spectroscopy: Probing the Entire Vibrational Spectrum in a Single Laser Shot with Femtosecond Time Resolution. *Opt. Lett.* **2012**, *37*, 2265−2267.

(38) Gowd, E. B.; Tashiro, K.; Ramesh, C. Structural Phase Transitions of Syndiotactic Polystyrene. *Prog. Polym. Sci.* **2009**, *34*, 280−315.

(39) Deak, J. C.; Pang, Y.; Sechler, T. D.; Wang, Z.; Dlott, D. D. Real-Time Detection of Vibrational Energy Transfer across a Molecular Layer: Reverse Micelles. *Science* **2004**, *306*, 473−476.

(40) Wang, Z. H.; Pang, Y. S.; Dlott, D. D. Hydrogen-Bond Disruption by Vibrational Excitations in Water. *J. Phys. Chem. A* **2007**, *111*, 3196−3208.

(41) Mukamel, S. *Principles of Nonlinear Optical Spectroscopy*; Oxford University Press: New York, 1995.

(42) Lawkowicz, J. *Principles of Fluorescence Spectroscopy*, 3rd ed.; Springer: New York, 2006.

(43) Valeur, B. *Molecular Fluorescence: Principles and Applications*; Wiley-VCH: Weinheim, Germany, 2002.

(44) Dong, F.; Miller, R. Vibrational Transition Moment Angles in Isolated Biomolecules: a Structural Tool. *Science* **2002**, *298*, 1227−1230.

(45) Kerr, K.; Ashmore, J. Structure and Conformation of Orthorhombic L-Cysteine. *Acta Crystallogr, Sect. B* **1973**, *29*, 2124−2127.

(46) Kerr, K.; Ashmore, J. P.; Koetzle, T. F. A Neutron Diffraction Study of L-Cysteine. *Acta Crystallogr., Sect. B* **1975**, *31*, 2022−2026.

(47) Ayyagari, C.; Bedrov, D.; Smith, G. D. Structure of Atactic Polystyrene: A Molecular Dynamics Simulation Study. *Macromolecules* **2000**, *33*, 6194−6199.

(48) Woo, E. M.; Sun, Y. S.; Yang, C. P. Polymorphism, Thermal Behavior, and Crystal Stability in Syndiotactic Polystyrene vs. Its Miscible Blends. *Prog. Polym. Sci.* **2001**, *26*, 945−983.

(49) Ishihara, N.; Seimiya, T.; Kuramoto, M.; Uoi, M. Crystalline Syndiotactic Polystyrene. *Macromolecules* **1986**, *19*, 2464−2465.

(50) Guerra, G.; Vitagliano, V. M.; De Rosa, C.; Petraccone, V.; Corradini, P. Polymorphism in Melt Crystallized Syndiotactic Polystyrene Samples. *Macromolecules* **1990**, *23*, 1539−1544.

(51) Chatani, Y.; Shimane, Y.; Inoue, Y.; Inagaki, T.; Ishioka, T.; Ijitsu, T.; Yukinari, T. Structural Study of Syndiotactic Polystyrene: 1. Polymorphism. *Polymer* **1992**, *33*, 488−492.

(52) De Rosa, C.; Rapacciuolo, M.; Guerra, G.; Petraccone, V.; Corradini, P. On the Crystal Structure of the Orthorhombic Form of Syndiotactic Polystyrene. *Polymer* **1992**, *33*, 1423−1428.

(53) Hew-Der, Wu; Tseng, C. R.; Chang, F. C. Chain Conformation and Crystallization Behavior of the Syndiotactic Polystyrene Nanocomposites Studied Using Fourier Transform Infrared Analysis. *Macromolecules* **2001**, *34*, 2992−2999.

(54) Wu, H. D.; Wu, S. C.; Wu, I. D.; Chang, F. C. Novel Determination of the Crystallinity of Syndiotactic Polystyrene Using FTIR Spectrum. *Polymer* **2001**, *42*, 4719−4725.

(55) Chatani, Y.; Shimane, Y.; Ijitsu, T.; Yukinari, T. Structural Study on Syndiotactic Polystyrene: 3. Crystal Structure of Planar Form I. *Polymer* **1993**, *34*, 1625−1629.

Relative Intermolecular Orientation Probed via Molecular Heat Transport

Hailong Chen, Hongtao Bian, Jiebo Li, Xiewen Wen, Junrong Zheng*
Department of Chemistry, Rice University, Houston, TX 77005, USA
* To whom correspondence should be addressed. Tel: 001-713-348-2048. E-mail: junrong@rice.edu

Supporting materials

Details of DFT calculation

To calculate the transition dipole moment directions of the vibrational modes in a polymer, it is usually not necessary to optimize the structure of an entire molecule, but only the structure and the vibrational modes for a subunit of the polymer are needed to be calculated. The reason is not just for the simplicity, but also necessary to calculate the cross angle between two coupled vibrational mode. The calculated vibrational modes for the entire molecule is always delocalized among different subunits, which means that the resulted vector direction is the sum of a several vibrational components located at different subunits. However, vibrational coupling signal is typically much larger for vibrations within the same subunit than in different units. As the result of this observation, calculating the vibrational modes for only a subunit of the polymer is sufficient for determined the vibrational cross angle.

According to the above analysis, we calculated the transition dipole moment directions of ring CH stretch (3060 cm^{-1}) and the ring CC stretch (1600 cm^{-1}) modes within a subunit of polystyrene. The optimized structure is shown in fig.S1. To further reduce the interference from the backbone CH involved vibrations. We replace all the hydrogen atoms at the backbone with deuterium atoms to shift their vibrational frequencies for calculation.

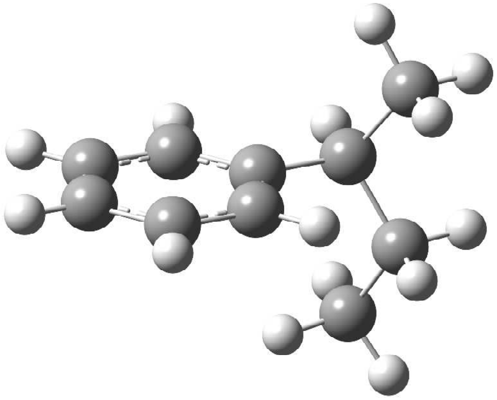

Figure S1. *The B3LYP/6-311++G(d,p) optimized structures of one subunit of polystyrene .*

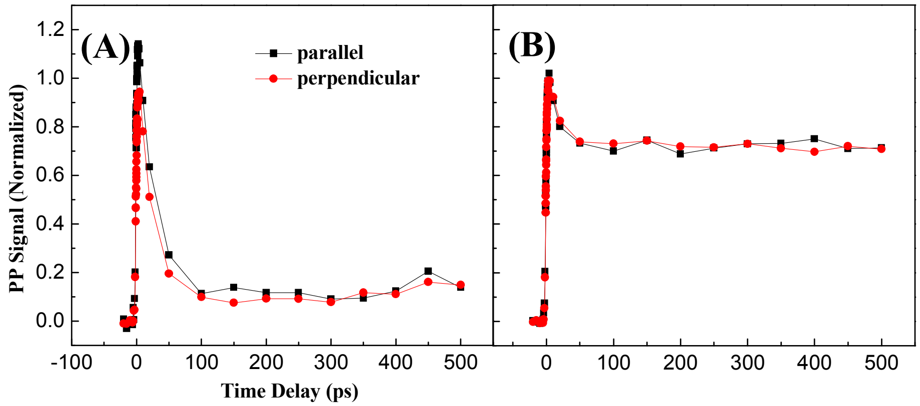

Figure S2. *Time dependent polarization selective intensities of peaks at* $\omega_1 = 3060 \text{ cm}^{-1}$, *and* $\omega_3 = 1600 \text{ cm}^{-1}$ *of (A) 2 wt % atactic polystyrene/chloroform solution, (B) sample 1. Each set of the data was norma*lized according to the initial *maximum of the total intensity P(t). The results show that the heat effect by exciting/detecting the same pair of modes in a 2 wt% polystyrene/chloroform solution is about 1/8 of that in the bulk polystyrene solid sample, indicating most of the heat generated by the vibrational relaxation from the polystyrene is transferred to the solvent rather than within polystyrene molecules. It demonstrate that the heat effects observed in the samples 1, 2 and 3 are mainly from the intermolecular rather than intramolecular heat transfer accompanying the vibrational relaxation of the initially excited mode.*

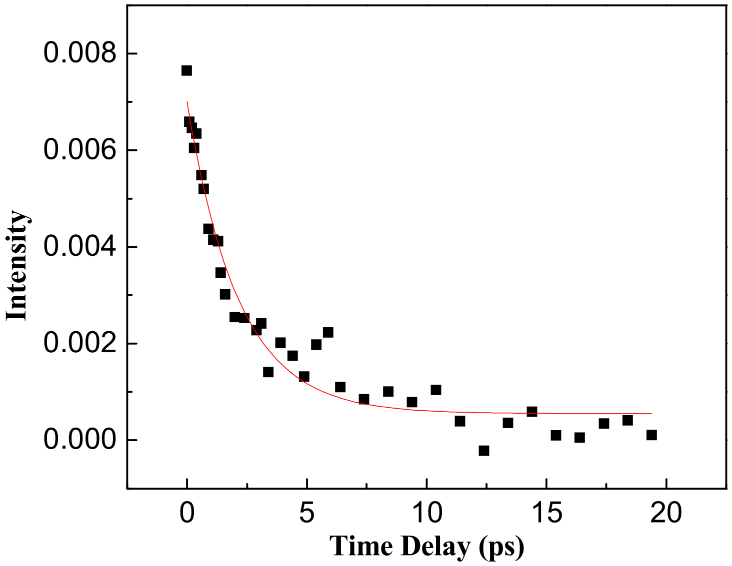

Figure S3. *Time dependent intensities ($P(t) = P_{\parallel}(t) + 2P_{\perp}(t)$) of peaks at* $\omega_1 = 3060\ \text{cm}^{-1}$*, and* $\omega_3 = 3060\ \text{cm}^{-1}$ *of sample 1 (points are data. Lines are fits), with the heat induced signal subtracted from the data. The fitting result indicates that the vibrational lifetime of the CH stretch is about 2.1 ±0.2 ps.*

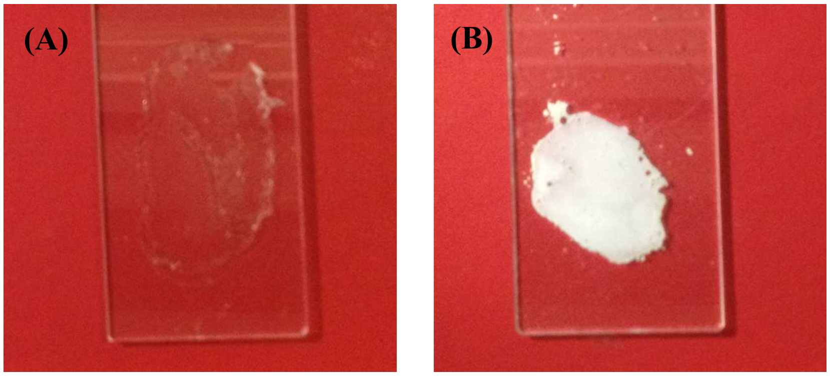

Figure S4. *Photographs of (A) sample 1 and (B) sample 3. The glassy sample 1 is transparent and the semicrystalline sample 3 is opaque.*

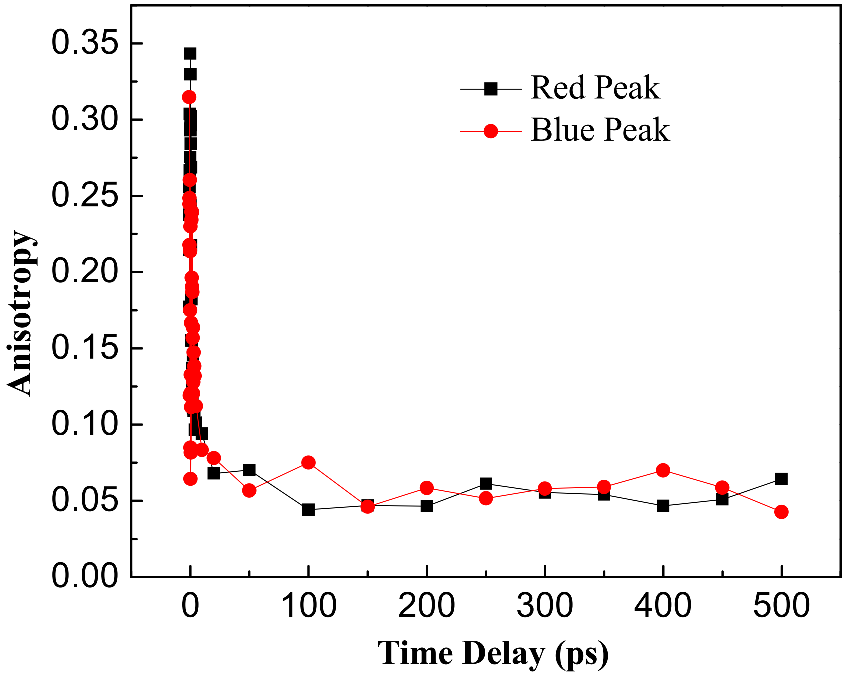

Figure S5. *Time dependent anisotropy values from red peak 3 (black) and blue peak 4 (red) in fig.8A.*